



## A Novel Low-Strain Phosphate Cathode for High-Rate and Ultralong Cycle-Life Potassium-Ion Batteries.

Item Type	Article
Authors	Zhou, Xiaosi;Liao, Jiaying;Chen, Cailing;Hu, Qiao;Du, Yichen;He, Yanan;Xu, Yifan;Zhang, Zhuangzhuang
Citation	Zhou, X., Liao, J., Chen, C., Hu, Q., Du, Y., He, Y., ... Zhang, Z. (2021). A Novel Low-Strain Phosphate Cathode for High-Rate and Ultralong Cycle-Life Potassium-Ion Batteries. <i>Angewandte Chemie International Edition</i> . doi:10.1002/anie.202112183
Eprint version	Post-print
DOI	<a href="https://doi.org/10.1002/anie.202112183">10.1002/anie.202112183</a>
Publisher	Wiley
Journal	Angewandte Chemie
Rights	Archived with thanks to Angewandte Chemie (International ed. in English)
Download date	2024-04-18 20:45:03
Link to Item	<a href="http://hdl.handle.net/10754/671928">http://hdl.handle.net/10754/671928</a>

## A Novel Low-Strain Phosphate Cathode for High-Rate and Ultralong Cycle-Life Potassium-Ion Batteries

Jiaying Liao<sup>+</sup>, Cailing Chen<sup>+</sup>, Qiao Hu, Yichen Du, Yanan He, Yifan Xu, Zhuangzhuang Zhang, and Xiaosi Zhou\*

[\*] Dr. J. Liao, Y. Du, Y. He, Y. Xu, Z. Zhang, Prof. X. Zhou  
School of Chemistry and Materials Science, Nanjing Normal University, Nanjing 210023, China  
E-mail: zhouxiaosi@njnu.edu.cn

Dr. C. Chen  
Advanced Membranes and Porous Materials Center, Physical Science and Engineering Division,  
King Abdullah University of Science and Technology (KAUST), Thuwal 23955-6900, Saudi Arabia

Dr. Q. Hu  
Institute of Nuclear and New Energy Technology, Tsinghua University, Beijing 100084, China

[<sup>+</sup>] These authors contributed equally to this work.

**Abstract:** Most potassium-ion battery (PIB) cathode materials have deficient structural stability because of the huge radius of potassium ion, leading to inferior cycling performance. In this work, we report the controllable synthesis of a novel low-strain phosphate material  $K_3(\text{VO})(\text{HV}_2\text{O}_3)(\text{PO}_4)_2(\text{HPO}_4)$  (denoted KVP) nanorulers as an efficient cathode for PIBs. The as-synthesized KVP nanoruler cathode can exhibit an initial reversible capacity of  $80.6 \text{ mAh g}^{-1}$  under  $20 \text{ mA g}^{-1}$ , with a large average working potential of  $4.11 \text{ V}$ . It can also manifest an excellent rate property of  $54.4 \text{ mAh g}^{-1}$  under  $5 \text{ A g}^{-1}$ , with an exceedingly high capacity preservation of  $92.1\%$  over 2500 cycles. The outstanding potassium storage capability of KVP nanoruler cathode originates from low-strain  $\text{K}^+$  uptake/removal mechanism, inherent semiconductor characteristic, and small  $\text{K}^+$  migration energy barrier. The high energy density and prolonged cyclic stability of KVP nanorulers//polyaniline-intercalated layered titanate full battery verifies the superiority of KVP nanoruler cathode in PIBs. Our results show that this high-voltage low-strain phosphate material is a competitive cathode for PIBs and will draw more attention and investigations in the future.

**Keywords:** phosphate materials; nanostructure; low-strain; cathode; potassium-ion batteries

## *Introduction*

Lithium-ion batteries (LIBs) are the state-of-the-art energy storage technologies for electric vehicles and portable devices due to their long cycle life and high energy density.<sup>[1,2]</sup> Nevertheless, the limited resource and ever-growing cost of lithium have impeded some implementations of LIBs, particularly in the field of large-scale energy storage for intermittent energy resources, including solar energy and wind energy.<sup>[3,4]</sup> In recent years, potassium-ion batteries (PIBs) have attracted extensive attention owing to the abundant potassium resources, the low redox potential of  $K^+/K$  ( $-2.93$  V vs. SHE), the weaker Lewis acidity of potassium ion and the resulting smaller solvated potassium ion radius, and the feasibility of graphite anode.<sup>[5-8]</sup> However, the large size of  $K^+$  ( $1.38$  Å) commonly brings about poor  $K^+$ -migration kinetics and apparent polarization.<sup>[9,10]</sup> Moreover, the huge ionic radius of  $K^+$  also results in tremendous lattice strain and remarkable volume variation during potassiation/depotassiation and thereby worsens the cyclic property of electrode materials.<sup>[11]</sup> As a result, it is of great importance to put forward reasonable design on electrodes with enhanced potassium ion diffusion dynamics and architectural stability for PIBs.

The positive electrode plays a pivotal role in the energy density and power density of the full battery, particularly the elevated potential positive electrode. Unfortunately, only a few types of positive electrodes for PIBs have been successfully designed and synthesized, including Prussian blue analogues,<sup>[12,13]</sup> organic materials,<sup>[14,15]</sup> layered transition-metal oxides,<sup>[16,17]</sup> and phosphate compounds.<sup>[18,19]</sup> Among diverse kinds of cathode materials for PIBs, phosphate compounds have received widespread investigations with high capacity and good cyclic performance on account of

their large interstitial channels and robust three-dimensional frameworks, which are favorable for obtaining superfast  $K^+$  migration kinetics and low-strain potassium-ion storage mechanism.<sup>[20]</sup> In addition, the phosphate compounds can be fabricated through simple synthesis procedures without elevated-temperature annealing, which would greatly diminish the synthesis cost.<sup>[21]</sup>

In terms of the component of phosphates, transition metals are the main elements to achieve diverse electrochemical features. V-based phosphates deliver higher working voltage and longer cyclic stability than Ti and Fe-based phosphates in  $K^+$  storage owing to the abundant changeable valence states from +2 to +5 and negligible volumetric variations during charging/discharging, which enable them one of most potential PIB cathode materials.<sup>[22-24]</sup> Recently, Lu's group has demonstrated a V-based phosphate material as an efficient PIB cathode.<sup>[25]</sup> Nonetheless, the V-based phosphate composite has been fabricated by high-temperature treatment, which substantially restricts its large-scale utilization. Additionally, the structural evolution of the V-based phosphate lacks systematic investigation, and its rate capability requires further improvement. Thus, it is highly desirable to exploit facile and scalable methods to boost the potassium storage properties of V-based phosphates and to fully understand their structural evolution mechanisms.

Herein, we demonstrate the controllable fabrication of a novel low-strain phosphate-based PIB cathode material  $K_3(VO)(HV_2O_3)(PO_4)_2(HPO_4)$  (denoted KVP) nanorulers via a one-step solvothermal method. The obtained KVP nanorulers manifest a high average working voltage (4.11 V), extraordinary cyclic performance (92.1% capacity preservation over 2500 cycles), and outstanding rate property ( $54.4 \text{ mAh g}^{-1}$  under  $5 \text{ A g}^{-1}$ ). In situ X-ray diffraction (XRD) technique is adopted to unveil the excellent architectural stability of KVP nanorulers upon repeated  $K^+$  de-/intercalation processes which shows that KVP possesses slight cell volume change (2.7%). The rapid

potassium-ion transportation kinetics is corroborated by electrochemical tests and density functional theory (DFT) calculations. Besides, a full battery is built by employing KVP nanorulers as the cathode and polyaniline-intercalated layered titanate as the anode, which displays a large energy density ( $\sim 236$  Wh  $\text{kg}^{-1}$ ) and long-term cyclic stability with 81.9% capacity retention after 600 cycles.

## Results and Discussion

The phase of the as-fabricated KVP nanorulers is examined by Rietveld refinement on XRD as shown in **Figure 1a** and **Tables S1** and **S2**. All diffraction peaks can be assigned to the space group of *Pnma* (62) with the lattice parameters  $a = 7.0212(1)$  Å,  $b = 13.5789(5)$  Å,  $c = 14.1750(3)$  Å. The Rietveld refinement also unraveled there are no obvious impurities in the KVP nanorulers. The molecular formula of KVP can be expressed as  $\text{K}_3(\text{VO})(\text{HV}_2\text{O}_3)(\text{PO}_4)_2(\text{HPO}_4)$ , which is further confirmed by thermogravimetric analysis (TGA; **Figure S1**) and inductively coupled plasma (**Table S3**). Raman spectrum of KVP in **Figure S2** demonstrates that the prominent peaks at 476 and 865  $\text{cm}^{-1}$  are attributed to the bending and stretching modes of the  $\text{PO}_4^{3-}$  group in  $[(\text{PO}_4)_2(\text{HPO}_4)]^{8-}$ , and the peaks at 757 and 963  $\text{cm}^{-1}$  correspond to V–O group.<sup>[26]</sup> FTIR spectrum of the KVP nanorulers is displayed in **Figure S3**. The broad peaks centered at 3458 and 1641  $\text{cm}^{-1}$  might be put down to two or more O–H stretching vibrations and bending vibrations, respectively.<sup>[27]</sup> These results imply the coexistence of V–O–H and P–O–H in the KVP sample, in accordance with the TGA analysis. The X-ray photoelectron spectrum in **Figure S4** validates that the valence of vanadium in KVP is tetravalent.

The morphology and microarchitecture of KVP are studied by field-emission scanning electron microscope (SEM) and transmission electron microscope (TEM). SEM and TEM observations reveal that the KVP product consists of uniform nanorulers with an average size of  $\sim 880$  nm  $\times$  260 nm  $\times$  63

nm (**Figure 1b–d**). The nanosized morphology is favorable for the  $K^+$  migration upon charging and discharging.<sup>[28–30]</sup> An upright-flat view (**Figure 1d**) shows that the as-synthesized KVP nanorulers have a dense structure without cavities or grain boundaries. Pure phase of an orthorhombic structure is further corroborated by selected area electron diffraction (SAED; inset in **Figure 1d** and **Figure S5**). Alternate tight and sparse array of K atoms are observed along the [001] zone axis in the spherical aberration corrected high-resolution TEM (HRTEM) image (**Figure 1e** and **Figure S6**), which shows good consistency with the atomic model of a single-crystalline KVP nanoruler (**Figure 1f** and **Figure S7**). Element mappings indicate a homogeneous distribution of K, V, P, and O elements with a stoichiometric ratio as designed in a single KVP nanoruler (**Figure 1g–i** and **Figures S8** and **S9**). Furthermore, the specific surface area of the KVP nanorulers is approximately  $15.7 \text{ m}^2 \text{ g}^{-1}$  (**Figure S10**), which is conducive to more sufficient contact between electrode and electrolyte, thereby improving the reaction kinetics.

The size and morphology of the products can also be regulated by tuning the volume ratio of ethylene glycol (EG) and water in the precursor solution (**Figures S11–S14**). Representatively, uniform KVP nanorulers (**Figure 1**) are obtained with an  $H_2O/EG$  ratio of 1/2. When an  $H_2O/EG$  ratio of 1/1 is used, KVP wide nanorulers (**Figure 2a,b**) with a mean size of  $\sim 940 \text{ nm} \times 470 \text{ nm} \times 110 \text{ nm}$  are gained (**Figures S15–S17**). **Figure S18** unravels that the (001) plane of KVP contains most oxygen atoms and a relatively low surface energy (**Table S4**). Through the hydrogen bonding between oxygen atoms and hydroxyls, EG molecules could be readily adsorbed on the (001) facet.<sup>[31]</sup> Thus, the KVP nanorulers with large (001) surfaces are formed through the solvent with EG as the main component. Nevertheless, when more  $H_2O$  is added into the reaction solvent, the selective adsorption of one hydroxyl group of  $H_2O$  is easier than that of two hydroxyl groups of EG.

Consequently, the (001) and (010) faces of KVP are readily adsorbed by H<sub>2</sub>O molecules via hydrogen bonding, leading to the formation of KVP wide nanorulers with an elongation along the [010] direction and a thick *c*-axis (**Figure 2a,b**). When the solvent system is composed of pure H<sub>2</sub>O, the H<sub>2</sub>O molecules are preferentially adsorbed on the (001), (010), and (102) faces of KVP through hydrogen bonding due to the lower surface energies on these planes. Therefore, KVP crystals with apparent (010) and (102) facets are generated and have a shape of rectangular prism microrod (that is, KVP microrods) with an average size of ~2.3 μm × 530 nm × 240 nm (**Figure 2c,d** and **Figures S19–S21**). Moreover, the concentration of VOSO<sub>4</sub> precursor solution also has a significant impact on the morphology and size of the products. More specifically, the KVP particles prepared with 0.32 M VOSO<sub>4</sub> solution present a microsphere architecture (diameter ~31 μm) constructed by nanorulers (that is, KVP microspheres; **Figure 2e,f** and **Figures S22** and **S23**), whereas the sample fabricated with 0.08 M VOSO<sub>4</sub> solution exhibits an irregular particle morphology (that is, KVP irregular particles; **Figures S24–S26**). **Figure S27** illustrates the XRD patterns of the KVP products synthesized under different synthesis conditions, demonstrating that these solvent compositions and precursor concentrations have no influence on the phase purity.

To achieve excellent potassium storage performance of KVP, we choose the carbonate- and sulfone-based electrolytes (1 M KPF<sub>6</sub> dissolved in propylene carbonate/ethylene carbonate (PC/EC, 1:1 by volume) and 5 M potassium bis(fluorosulfonyl)imide (KFSI) dissolved in tetramethylene sulfone (TMS)) and make a comparison (**Figure S28**).<sup>[32]</sup> **Figure 3a** shows the cyclic voltammetry (CV) behavior of the KVP nanorulers in the above two electrolytes. In the TMS-based electrolyte, the KVP nanoruler cathode displays a pair of perfectly-shaped redox peaks with small potential polarization. By contrast, the KVP nanoruler cathode faced much larger polarization in the carbonate-

based electrolyte. **Figure 3b** shows that the voltage hysteresis of the KVP nanoruler cathode in the TMS-based electrolyte (126 mV) is distinctly lower than that in the carbonate-based electrolyte (277 mV). The smaller voltage hysteresis of the KVP nanorulers/K half-batteries in the TMS-based electrolyte stems from the decreased polarization of potassium stripping/plating (**Figure S29**). The KVP nanorulers afford a larger reversible capacity of  $80.6 \text{ mAh g}^{-1}$  than that of the KVP wide nanorulers ( $69.1 \text{ mAh g}^{-1}$ ) and KVP microrods ( $50.8 \text{ mAh g}^{-1}$ ) (**Figure S30**) with a large average working potential of 4.11 V in the TMS-based electrolyte, consistent with the theoretical redox potentials obtained from first-principles calculations (**Figure S31**). The initial Coulombic efficiency (CE) is approximately 62%, which is largely due to the initial dehydrogenation of KVP nanorulers (**Figures S32 and S33**), resulting in that the discharge capacity of KVP nanorulers is relatively inferior to that of Ti- and Fe-based phosphates.<sup>[18,24]</sup> In terms of the working voltage, the KVP nanoruler electrode surpasses most previously reported PIB cathode materials (**Figure 3c**).<sup>[13,17,20,28,29,33-37]</sup>

**Figure 3d** illustrates the rate property of KVP nanorulers cycled at different current densities. When measured at 0.02, 0.05, 0.1, 0.2, 0.5, 1 and 2  $\text{A g}^{-1}$ , average discharge capacities of 80.8, 79.4, 78.0, 75.5, 72.7, 67.6, and 60.8  $\text{mAh g}^{-1}$  can be delivered. Even when a high current rate of 5  $\text{A g}^{-1}$  is executed, a decent capacity of 54.4  $\text{mAh g}^{-1}$  is still maintained. In sharp contrast, the capacity of KVP microrods drops dramatically with the elevation of current density. The charge/discharge profiles at various current densities further verify the prominent rate capability of KVP nanorulers (**Figure 3e**). Furthermore, the KVP nanoruler electrode also presents superior cyclic stability. Specifically, 93.5% of the initial capacity is maintained after 200 depotassiation/potassiation cycles under 0.1  $\text{A g}^{-1}$  (**Figure 3f** and **Figure S34**). The CE of the KVP nanorulers is preserved at about

98.5% during cycling. On the contrary, the reversible capacities of KVP microrods are lower. The KVP wide nanorulers show much better cycling performance than the KVP microrods, thus suggesting the promoted electrochemical reaction by thinning the KVP crystal. The cycling and rate performances of KVP nanorulers are also superior to those of KVP microspheres and KVP irregular particles (**Figures S35 and S36**). It is worth mentioning that the architectures and morphologies of KVP samples are still well-retained after 200 cycles (**Figures S37–S44**). In addition, the KVP nanoruler electrode delivers a high capacity preservation of 92.1% over 2500 cycles under 500 mA g<sup>-1</sup> (**Figure 3g**). Meanwhile, the KVP nanoruler cathode demonstrates outstanding voltage steady during repetitive K<sup>+</sup> extraction/insertion (**Figure S45**). The potassium storage properties of KVP nanorulers outperform those of many reported PIB cathode materials, implying that the KVP nanorulers are a kind of PIB cathode material with great application potential (**Table S5**).<sup>[13,15,17,18,20,28,35,38]</sup> Moreover, the K<sup>+</sup> storage mechanism of KVP nanorulers is studied through CV examinations at diverse sweep speeds (**Figure S46a**). The results evidence that the potassium storage reaction involves both faradic process (oxidation/reduction reaction) and non-faradic process (pseudocapacitance) (**Figure S46b–d**).

To elucidate the structural evolution of KVP nanorulers as a cathode in PIBs, in situ XRD patterns are recorded based on a half-battery upon depotassiation/potassiation (**Figure S47**). As illustrated in **Figure 4a,b**, the (101), (212), (203), and (213) peaks of KVP nanorulers progressively shift to low angles, whereas the (024), (042), (141), and (142) peaks gradually divert toward high angles during depotassiation. These phenomena are ascribed to the expansion of the *a* axis and the contraction of the *b–c* plane, which originate from the increased electrostatic repulsion between the oxygen-containing polyhedrons when potassium ions are deintercalated. It is worth noting that the peak

movements are finite and in opposite directions, indicating the small volume variation upon  $K^+$  removal.<sup>[39]</sup> Furthermore, no other phases except orthorhombic phase are observed during depotassiation, suggestive of a solid-solution reaction mechanism. After discharging to 2.0 V, the peaks return to their original positions, signifying the high reversibility upon  $K^+$  uptake/release. The volume change and lattice parameters during  $K^+$  extraction/insertion are shown in **Figure 4c**. The volume change in the initial stage (corresponding to stage I in **Figure 4a**) is extremely small and irreversible, which is mainly caused by the dehydrogenation reaction. The KVP nanorulers attain ultrasmall cell volume change (2.7%) during the depotassiation/potassiation process, which are significantly lower than those of reported PIB cathodes (**Figure S48**).<sup>[20,21,28,38,40]</sup> Besides, a XRD pattern of the KVP nanoruler cathode after the ultralong cycling test is collected, demonstrating the well-preserved crystal architecture (**Figure S49**). These results indicate the outstanding structural stability of KVP nanorulers, which endows them with ultralong cycle life.

Apart from in situ XRD, synchrotron-based X-ray absorption spectra (XAS) are also gathered to monitor the mean vanadium valence and its local architecture evolution. **Figure S50** depicts a representative galvanostatic charging–discharging curves of the KVP nanoruler cathode, and the colored solid circles stand for the status of performing ex situ XAS measurements. **Figure 4d,e** show the V K-edge X-ray absorption near-edge spectra (XANES) upon  $K^+$  extraction/insertion, respectively. In order to better analyze the K-edge change of V, we define the energy with a normalized intensity of 0.5 as  $E_{0.5}$  and track the change of  $E_{0.5}$ .<sup>[41]</sup> It can be clearly seen that the V K-edge XANES spectra (**Figure 4d**) continuously move to higher energy during  $K^+$  deintercalation, which is correlated with the oxidation of vanadium ion during charging.<sup>[42]</sup> The energy shift of the V K-edge is around 1.19 eV. By comparing with  $V_2O_4$  and  $V_2O_5$  standard sample, it can be deduced

that the V valence has changed from 4.3+ to 5+. A reverse shift is observed during  $K^+$  intercalation (**Figure 4e**), corresponding to the transformation of  $V^{5+}$  into  $V^{4.3+}$  during discharging. Obviously, the variation of XANES spectra in a whole cycle demonstrates the high valence reversibility of V in the KVP nanorulers. **Figure S51** presents the concerned  $k^2$ -weighted Fourier-transformed spectra of extended synchrotron X-ray absorption fine-structure (EXAFS). The broad peak located at 1.0–2.1 Å belongs to V–O octahedral coordination. It is noticed that V–O distance progressively shrinks along depotassiation process and elongates along potassiation process. The perfect coincidence of XANES and EXAFS profiles of the initial charge state and the final state of discharge indicate the excellent reversibility of vanadium environment (**Figures S52 and S53**). Integrating XANES and EXAFS curves, it is testified the  $V^{4.3+}/V^{5+}$  redox reaction takes place and is considerably reversible during  $K^+$  uptake/removal process in the KVP nanoruler cathode in the voltage range of 2.0–4.8 V.

To gain some further insight into the remarkable rate behavior of KVP nanorulers in TMS-based electrolyte, we perform a kinetic investigation based on galvanostatic intermittent titration technique (GITT) measurements. **Figure 4f** renders the charging/discharging GITT profiles after reaching thermodynamic equilibrium (10 cycles). As plotted in **Figure S54**, the cell voltage  $E$  is linearly associated with the square root of galvanostatic time ( $\tau^{1/2}$ ). The potassium ion diffusion kinetic is represented by chemical diffusion coefficients ( $D_{K^+}$ ). The result demonstrates the  $D_{K^+}$  value changes with the depth of depotassiation/potassiation (**Figure S55**). Noticeably, the  $D_{K^+}$  values of KVP nanorulers calculated from the GITT curves are in the range from  $10^{-11}$  to  $10^{-9}$   $\text{cm}^2 \text{s}^{-1}$ , which are much larger than those of KVP wide nanorulers and KVP microrods and most reported PIB cathode materials, reflecting the rapid  $K^+$  diffusion dynamics (**Figures S56 and S57 and Table S6**).<sup>[28,40,43]</sup> The large  $K^+$  diffusion coefficient expounds well the superior rate property of KVP nanorulers.

Furthermore, the small charge-transfer resistance of the KVP nanoruler electrode is also conducive to enhancing the rate capability (**Figure S58**).

In order to deeply explore the intrinsic nature of the unique KVP nanoruler architecture that possesses superior rate capability, DFT calculations are conducted to determine the migration energy barriers of  $K^+$  along different directions (**Figure 4g** and **Figure S59**). From **Figure 4h**, it can be noticed that the potassium-ion diffusion energy barriers are all less than 0.55 eV, which are all highly effective migration pathways for KVP materials, providing a strong evidence for this newly developed phosphate-type PIB cathode with three-dimensional  $K^+$  diffusion channels.<sup>[44]</sup> Additionally, KVP has the smallest migration energy barrier of 0.3 eV along the *c* orientation, so that the thinnest sample KVP nanorulers exhibits the best rate performance in comparison with other KVP samples and PIB cathode materials. The total density of states (DOS) of pristine and charged KVP nanorulers reveal a semiconductor feature of KVP nanorulers (**Figure 4i** and **Figure S60**).

Considering the high flammability of metal K in practical applications, a prototype potassium-ion full battery is configured by assembling the KVP nanoruler cathode with a polyaniline-intercalated layered titanate (denoted PANI-LT, **Figures S61–S68**) anode. **Figure 5a** shows the working mechanism of the full battery, in which  $K^+$  deintercalates from the KVP nanoruler cathode and intercalates into the PANI-LT anode upon depotassiation, and a reverse electrochemical reaction happens upon the subsequent potassiation. **Figure S69** illustrates that one single potassium-ion full battery can power a "PIB" logo constructed by 31 light-emitting diode (LED) bulbs. The representative charging–discharging profiles of the full battery are displayed in **Figure 5b**. The KVP nanorulers//PANI-LT full battery manifests a high initial reversible capacity of 77.2 mAh  $g^{-1}$  under 20 mA  $g^{-1}$  (on the basis of the mass of the cathode) and a mean working voltage of approximately

3.06 V. As shown in **Figure S70**, the representative CV profile of the full battery demonstrates a pair of reversible redox peaks with a low voltage hysteresis.

The rate capability of the KVP nanorulers//PANI-LT full battery is presented in **Figure 5c**, reaching a discharge capacity of 78.1, 73.9, 69.5, 64.1, 57.4, and 51.0 mAh g<sup>-1</sup> at a current density from 0.02 to 1.0 A g<sup>-1</sup>. When the current rate drops to 0.02 A g<sup>-1</sup>, the reversible capacity can be restored to 77.8 mAh g<sup>-1</sup>, showing its excellent rate performance. In addition, the full battery exhibits a high initial discharge capacity of ~66.5 mAh g<sup>-1</sup> and remains stable with a good capacity maintenance of 81.9% over 600 cycles under 100 mA g<sup>-1</sup> (**Figure 5d**). The energy density of the full battery is estimated to be around 236 Wh kg<sup>-1</sup>. The galvanostatic charge/discharge profiles at the 2nd, 3rd, 10th, 100th, and 200th cycles nearly overlap (**Figure 5e**), indicative of the outstanding cyclic stability of our full cell. As compared to the reported potassium-in full batteries (**Table S7**), the KVP nanorulers//PANI-LT full cell delivers the optimal potassium storage comprehensive properties.<sup>[7,8,13,17,28,36,38-40,45]</sup> These results demonstrate the great potential of KVP nanorulers toward large-scale energy storage.

## Conclusion

In summary, a facile solvothermal strategy has been designed for the rational synthesis of KVP nanorulers. The KVP nanoruler cathode yields a high working voltage of 4.11 V, remarkable rate capability of 54.4 mAh g<sup>-1</sup> at 5 A g<sup>-1</sup>, and superior cycling stability with 92.1% capacity retention after 2500 cycles. The negligible volume variation during depotassiation/potassiation is revealed through in situ XRD measurements. The outstanding rate property could be attributed to the small potassium ion migration energy barrier of KVP nanorulers. Moreover, a potassium-ion full battery is

successfully built by combining the KVP nanoruler cathode with the PANI-LT anode, which exhibits a high working voltage of  $\sim 3.06$  V, a large energy density of  $236 \text{ Wh kg}^{-1}$ , and excellent cyclic stability with a capacity retention of 81.9% over 600 cycles. This study may provide some inspiration for the design and fabrication of advanced cathode materials for PIBs.

## Acknowledgements

This work was supported by the National Natural Science Foundation of China (22179603).

## References

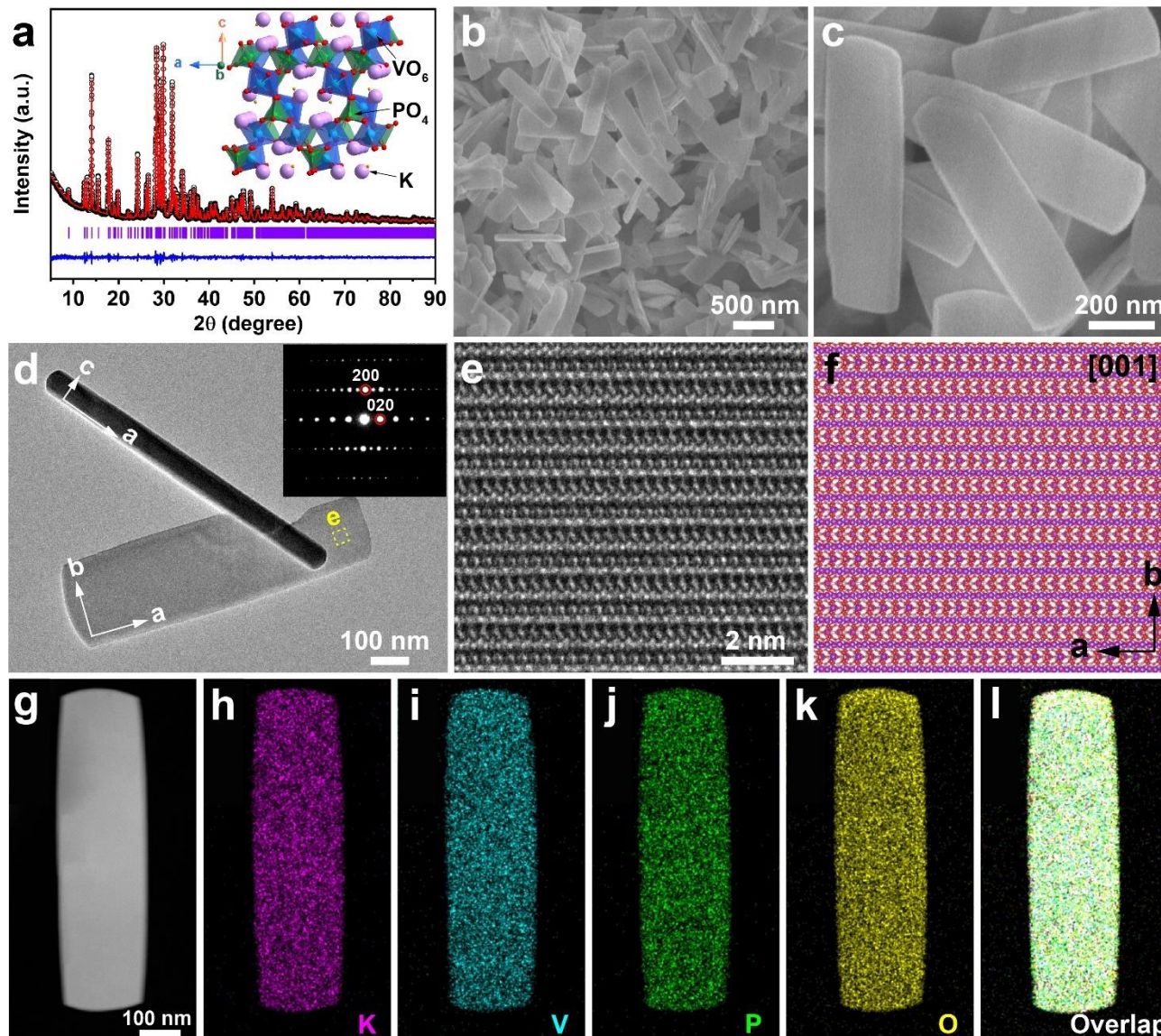
- [1] B. Dunn, H. Kamath, J.-M. Tarascon, *Science* **2011**, *334*, 928–935.
- [2] Y. Cao, M. Li, J. Lu, J. Liu, K. Amine, *Nat. Nanotechnol.* **2019**, *14*, 200–207.
- [3] J. B. Goodenough, K.-S. Park, *J. Am. Chem. Soc.* **2013**, *135*, 1167–1176.
- [4] Y. Fang, Y. Zeng, Q. Jin, X. F. Lu, D. Luan, X. Zhang, X. W. Lou, *Angew. Chem. Int. Ed.* **2021**, *60*, 8515–8520; *Angew. Chem.* **2021**, *133*, 8596–8601.
- [5] Z. Jian, W. Luo, X. Ji, *J. Am. Chem. Soc.* **2015**, *137*, 11566–11569.
- [6] T. Hosaka, K. Kubota, A. S. Hameed, S. Komaba, *Chem. Rev.* **2020**, *120*, 6358–6466.
- [7] X. Ge, S. Liu, M. Qiao, Y. Du, Y. Li, J. Bao, X. Zhou, *Angew. Chem. Int. Ed.* **2019**, *58*, 14578–14583; *Angew. Chem.* **2019**, *131*, 14720–14725.
- [8] L. Jiang, Y. Lu, C. Zhao, L. Liu, J. Zhang, Q. Zhang, X. Shen, J. Zhao, X. Yu, H. Li, X. Huang, L. Chen, Y.-S. Hu, *Nat. Energy* **2019**, *4*, 495–503.
- [9] W. Zhang, Y. Liu, Z. Guo, *Sci. Adv.* **2019**, *5*, eaav7412.
- [10] Y. Xu, Y. Du, Z. Yi, Z. Zhang, C. Lai, J. Liao, X. Zhou, *J. Energy Chem.* **2021**, *58*, 593–601.
- [11] Z. Sun, Y. Liu, W. Ye, J. Zhang, Y. Wang, Y. Lin, L. Hou, M.-S. Wang, C. Yuan, *Angew. Chem. Int. Ed.* **2021**, *60*, 7180–7187; *Angew. Chem.* **2021**, *133*, 7256–7263.
- [12] Y.-H. Zhu, Y.-B. Yin, X. Yang, T. Sun, S. Wang, Y.-S. Jiang, J.-M. Yan, X.-B. Zhang, *Angew. Chem. Int. Ed.* **2017**, *56*, 7881–7885; *Angew. Chem.* **2017**, *129*, 7989–7993.
- [13] L. Deng, J. Qu, X. Niu, J. Liu, J. Zhang, Y. Hong, M. Feng, J. Wang, M. Hu, L. Zeng, Q. Zhang,

- L. Guo, Y. Zhu, *Nat. Commun.* **2021**, *12*, 2167.
- [14] Q. Zhao, J. Wang, Y. Lu, Y. Li, G. Liang, J. Chen, *Angew. Chem. Int. Ed.* **2016**, *55*, 12528–12532; *Angew. Chem.* **2016**, *128*, 12716–12720.
- [15] Y. Hu, Y. Gao, L. Fan, Y. Zhang, B. Wang, Z. Qin, J. Zhou, B. Lu, *Adv. Energy Mater.* **2020**, *10*, 2002780.
- [16] Y.-S. Xu, S.-J. Guo, X.-S. Tao, Y.-G. Sun, J. Ma, C. Liu, A.-M. Cao, *Adv. Mater.* **2021**, *33*, 2100409.
- [17] T. Deng, X. Fan, C. Luo, J. Chen, L. Chen, S. Hou, N. Eidson, X. Zhou, C. Wang, *Nano Lett.* **2018**, *18*, 1522–1529.
- [18] S. S. Fedotov, N. D. Luchinin, D. A. Aksyonov, A. V. Morozov, S. V. Ryazantsev, M. Gaboardi, J. R. Plaisier, K. J. Stevenson, A. M. Abakumov, E. V. Antipov, *Nat. Commun.* **2020**, *11*, 1484.
- [19] J. Liao, Q. Hu, X. He, J. Mu, J. Wang, C. Chen, *J. Power Sources* **2020**, *451*, 227739.
- [20] H. Kim, D.-H. Seo, M. Bianchini, R. J. Clement, H. Kim, J. C. Kim, Y. Tian, T. Shi, W.-S. Yoon, G. Ceder, *Adv. Energy Mater.* **2018**, *8*, 1801591.
- [21] H. Park, H. Kim, W. Ko, J. H. Jo, Y. Lee, J. Kang, I. Park, S.-T. Myung, J. Kim, *Energy Storage Mater.* **2020**, *28*, 47–54.
- [22] M. Ohara, A. S. Hameed, K. Kubota, A. Katogi, K. Chihara, T. Hosaka, S. Komaba, *Chem. Sci.* **2021**, <https://doi.org/10.1039/d1sc03725k>.
- [23] R. Zhang, J. Huang, W. Deng, J. Bao, Y. Pan, S. Huang, C.-F. Sun, *Angew. Chem. Int. Ed.* **2019**, *58*, 16474–16479; *Angew. Chem.* **2019**, *131*, 16626–16631.
- [24] I. Sultana, M. M. Rahman, S. Mateti, N. Sharma, S. Huang, Y. Chen, *Batteries Supercaps* **2020**, *3*, 450–455.
- [25] Z. Liu, J. Wang, B. Lu, *Sci. Bull.* **2020**, *65*, 1242–1251.
- [26] R. L. Frost, Y. Xi, R. Scholz, A. Lopez, F. M. Belotti, *Vib. Spectrosc.* **2013**, *66*, 69–75.
- [27] E. Boivin, J.-N. Chotard, M. Menetrier, L. Bourgeois, T. Bamine, D. Carlier, F. Fauth, E. Suard, C. Masquelier, L. Croguennec, *J. Mater. Chem. A* **2016**, *4*, 11030–11045.
- [28] L. Li, Z. Hu, Y. Lu, C. Wang, Q. Zhang, S. Zhao, J. Peng, K. Zhang, S.-L. Chou, J. Chen, *Angew. Chem. Int. Ed.* **2021**, *60*, 13050–13056; *Angew. Chem.* **2021**, *133*, 13160–13166.
- [29] R. Xu, Y. Yao, H. Wang, Y. Yuan, J. Wang, H. Yang, Y. Jiang, P. Shi, X. Wu, Z. Peng, Z.-S. Wu, J. Lu, Y. Yu, *Adv. Mater.* **2020**, *32*, 2003879.

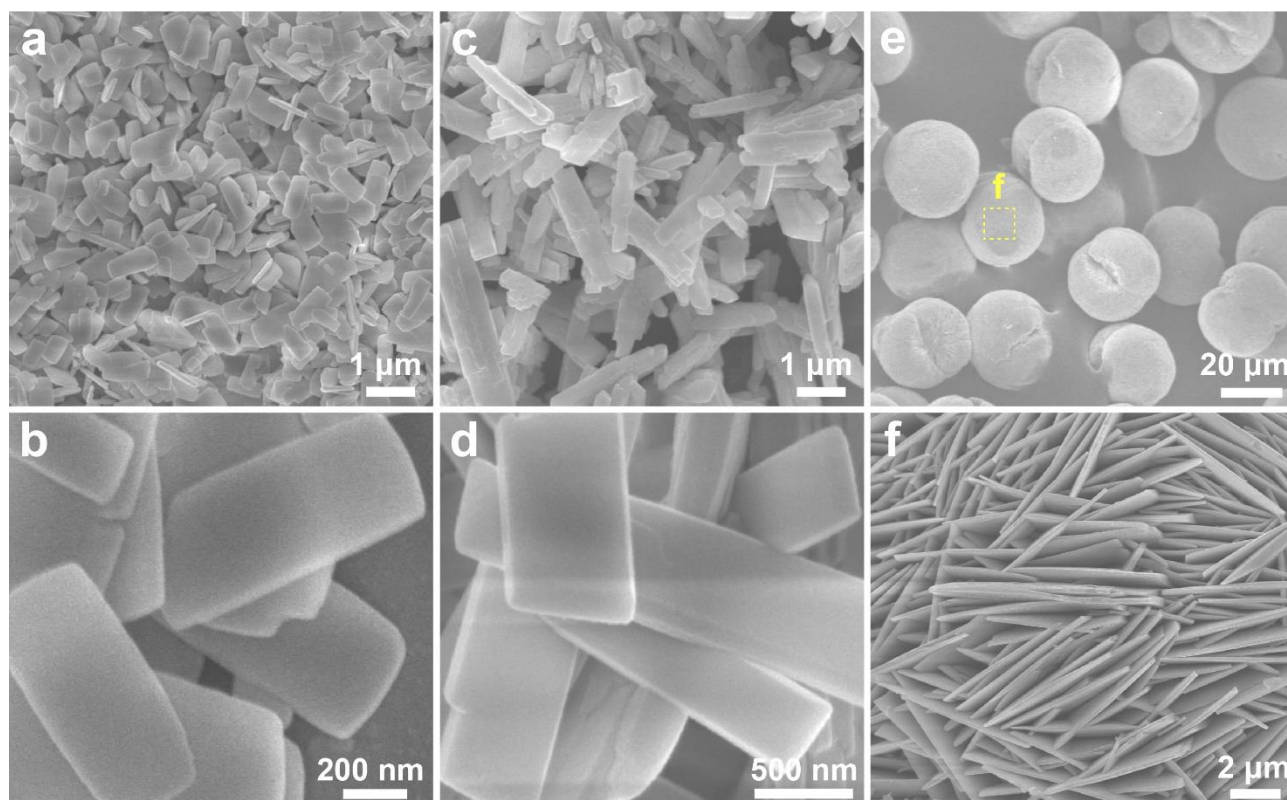
- [30] Z. Zhang, Y. Du, Q.-C. Wang, J. Xu, Y.-N. Zhou, J. Bao, J. Shen, X. Zhou, *Angew. Chem. Int. Ed.* **2020**, *59*, 17504–17510; *Angew. Chem.* **2020**, *132*, 17657–17663.
- [31] Z. Ma, G. Shao, Y. Fan, G. Wang, J. Song, T. Liu, *ACS Appl. Mater. Interfaces* **2014**, *6*, 9236–9244.
- [32] X. Li, X. Ou, Y. Tang, *Adv. Energy Mater.* **2020**, *10*, 2002567.
- [33] X. Ge, H. Di, P. Wang, X. Miao, P. Zhang, H. Wang, J. Ma, L. Yin, *ACS Nano* **2020**, *14*, 16022–16035.
- [34] Y. Chen, W. Luo, M. Carter, L. Zhou, J. Dai, K. Fu, S. Lacey, T. Li, J. Wan, X. Han, Y. Bao, L. Hu, *Nano Energy* **2015**, *18*, 205–211.
- [35] L.-W. Luo, C. Zhang, P. Xiong, Y. Zhao, W. Ma, Y. Chen, J. H. Zeng, Y. Xu, J.-X. Jiang, *Sci. China Chem.* **2021**, *64*, 72–81.
- [36] T. Deng, X. Fan, J. Chen, L. Chen, C. Luo, X. Zhou, J. Yang, S. Zheng, C. Wang, *Adv. Funct. Mater.* **2018**, *28*, 1800219.
- [37] J. Han, G.-N. Li, F. Liu, M. Wang, Y. Zhang, L. Hu, C. Dai, M. Xu, *Chem. Commun.* **2017**, *53*, 1805–1808.
- [38] B. Lin, X. Zhu, L. Fang, X. Liu, S. Li, T. Zhai, L. Xue, Q. Guo, J. Xu, H. Xia, *Adv. Mater.* **2019**, *31*, 1900060.
- [39] Z. Xiao, J. Meng, F. Xia, J. Wu, F. Liu, X. Zhang, L. Xu, X. Lin, L. Mai, *Energy Environ. Sci.* **2020**, *13*, 3129–3137.
- [40] B. Ji, W. Yao, Y. Zheng, P. Kidkhunthod, X. Zhou, S. Tunmee, S. Sattayaporn, H.-M. Cheng, H. He, Y. Tang, *Nat. Commun.* **2020**, *11*, 1225.
- [41] Q.-C. Wang, J.-K. Meng, X.-Y. Yue, Q.-Q. Qiu, Y. Song, X.-J. Wu, Z.-W. Fu, Y.-Y. Xia, Z. Shadike, J. Wu, X.-Q. Yang, Y.-N. Zhou, *J. Am. Chem. Soc.* **2019**, *141*, 840–848.
- [42] M. Chen, W. Hua, J. Xiao, D. Cortie, X. Guo, E. Wang, Q. Gu, Z. Hu, S. Indris, X.-L. Wang, S.-L. Chou, S.-X. Dou, *Angew. Chem. Int. Ed.* **2020**, *59*, 2449–2456; *Angew. Chem.* **2020**, *132*, 2470–2477.
- [43] W. B. Park, S. C. Han, C. Park, S. U. Hong, U. Han, S. P. Singh, Y. H. Jung, D. Ahn, K.-S. Sohn, M. Pyo, *Adv. Energy Mater.* **2018**, *8*, 1703099.
- [44] S. S. Fedotov, N. A. Kabanova, A. A. Kabanov, V. A. Blatov, N. R. Khasanova, E. V. Antipov, *Solid State Ionics* **2018**, *314*, 129–140.

- [45] L. Wang, B. Zhang, B. Wang, S. Zeng, M. Zhao, X. Sun, Y. Zhai, L. Xu, *Angew. Chem. Int. Ed.* **2021**, *60*, 15381–15389; *Angew. Chem.* **2021**, *133*, 15509–15517.

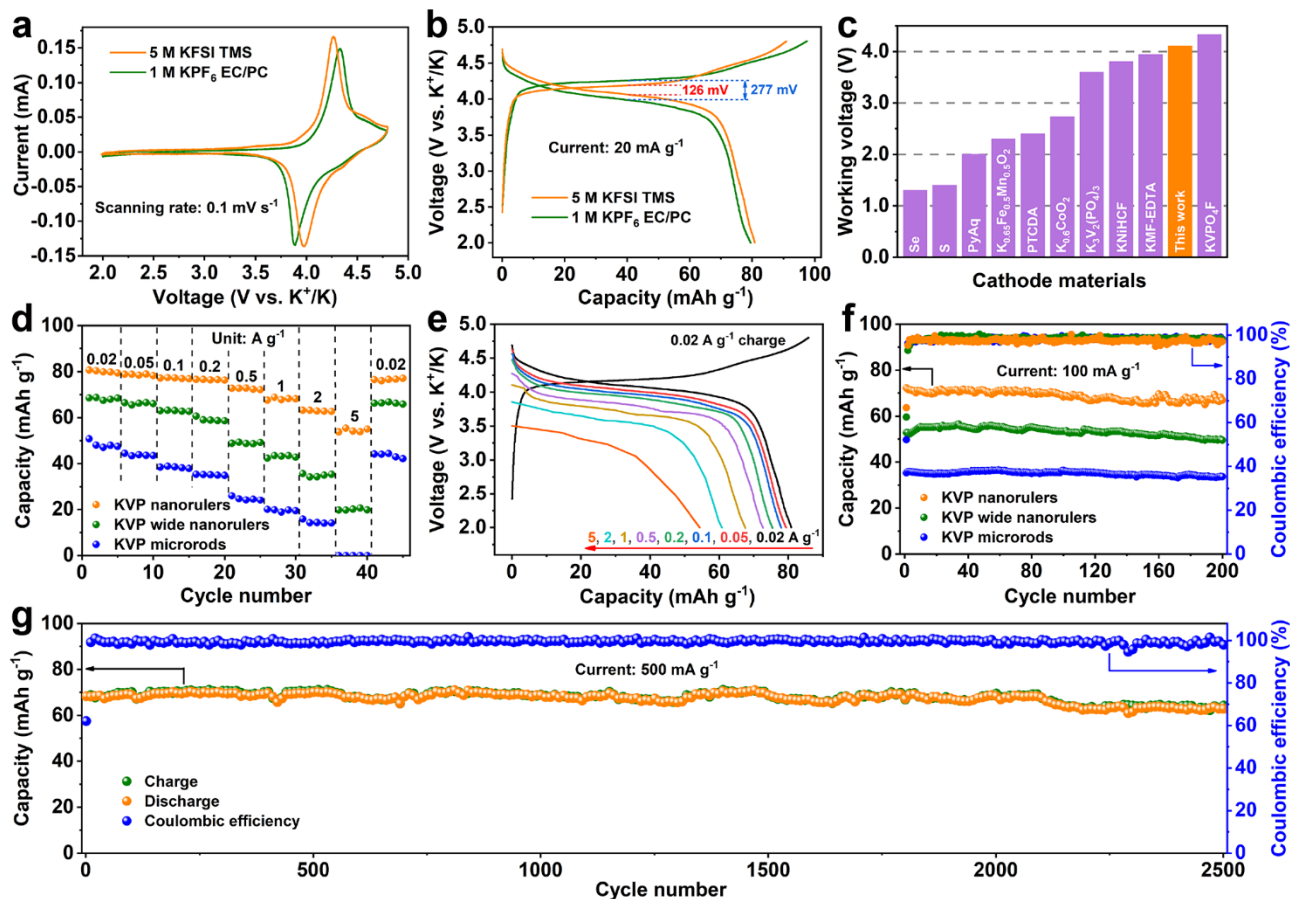
## Figures and captions



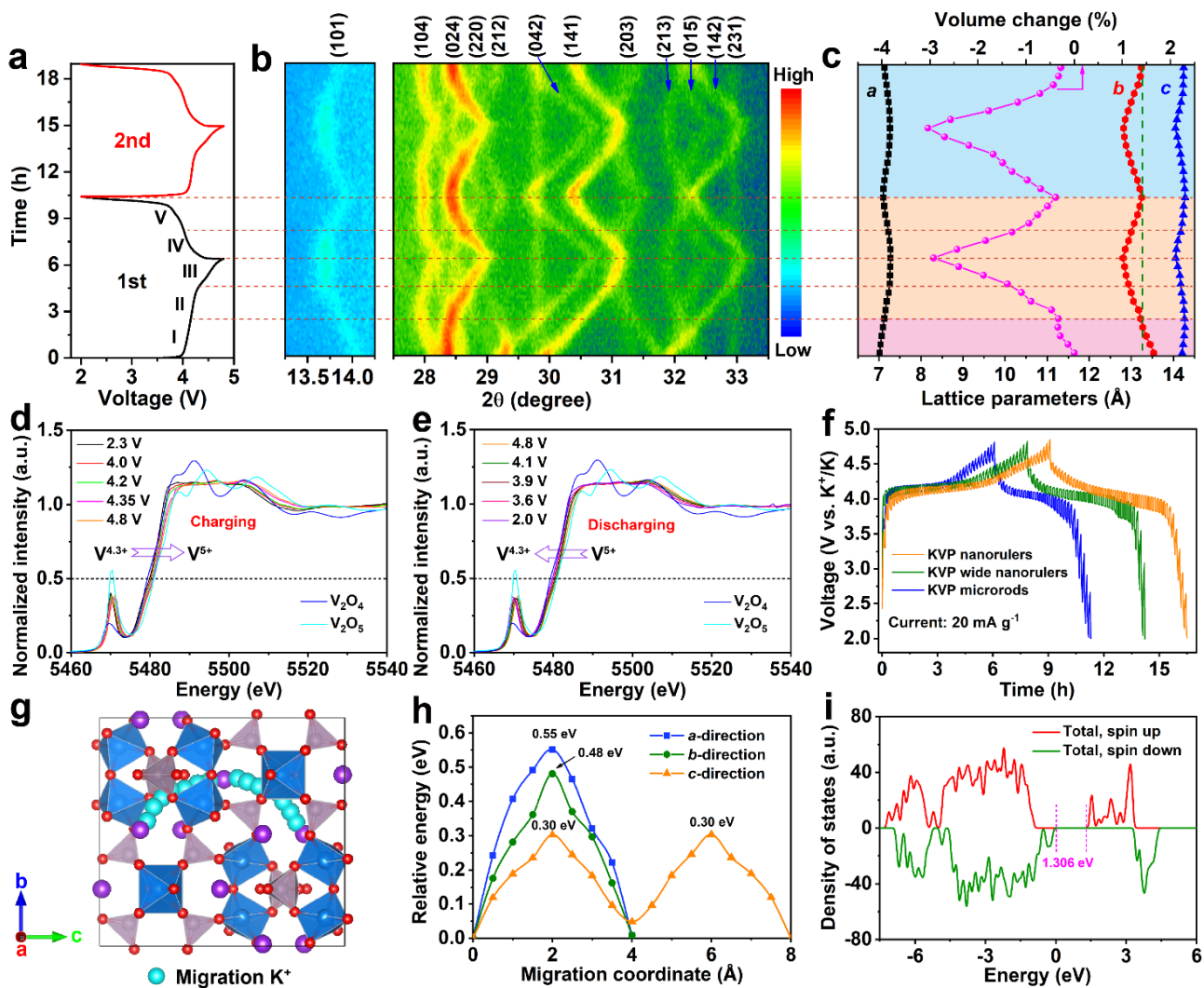
**Figure 1.** a) Rietveld refinement on XRD pattern, b),c) SEM images, d) TEM image, e),f) HRTEM image and atomic model, g) STEM image, and h)–k) the corresponding elemental distributions of KVP nanorulers. Insets in (a, d): schematic crystal structure and SAED pattern of KVP nanorulers.



**Figure 2.** a),b) FESEM images of KVP wide nanorulers. c),d) FESEM images of KVP microrods. e) FESEM image of KVP microspheres. f) Higher-magnification view corresponding to the region encircled by the yellow dotted square in (e).

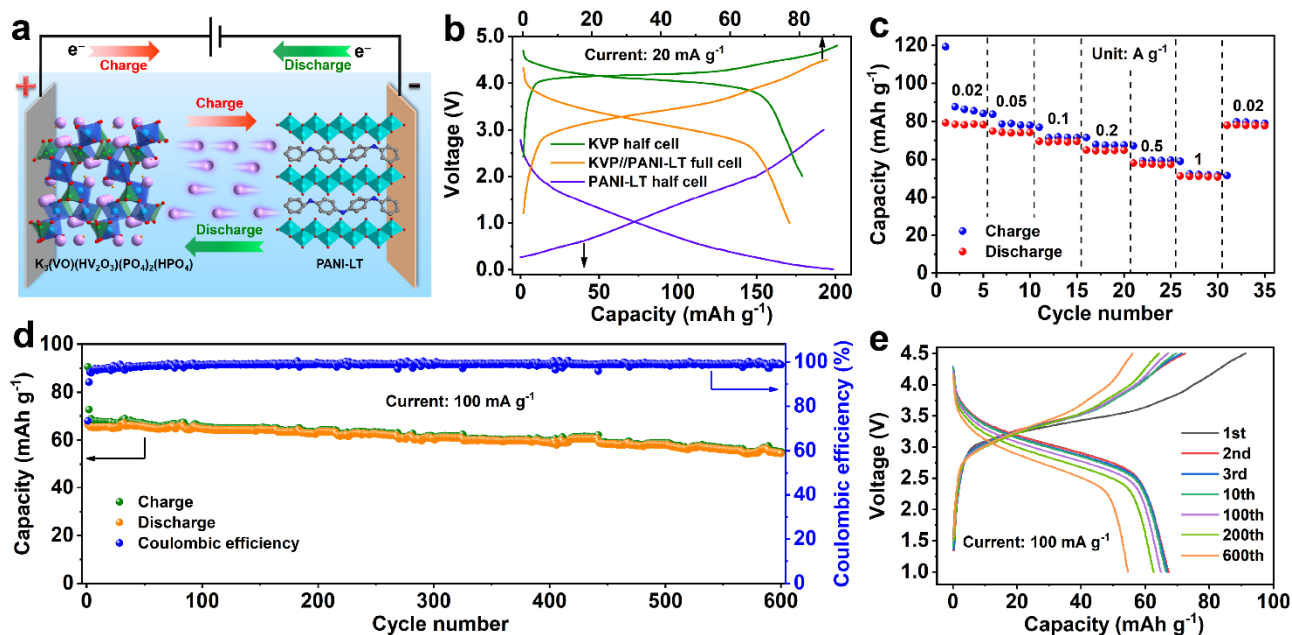


**Figure 3.** a) CV and b) charging/discharging profiles of the KVP nanoruler cathode. c) Comparison of working voltages of the KVP nanorulers with previously reported PIB cathode materials (S,<sup>[33]</sup> Se,<sup>[29]</sup> 3,4,9,10-perylene-tetracarboxylicacid-dianhydride (PTCDA),<sup>[34]</sup> poly(pyrene-*co*-anthraquinone) (PyAq),<sup>[35]</sup>  $\text{K}_{0.6}\text{CoO}_2$ ,<sup>[17]</sup>  $\text{K}_{0.65}\text{Fe}_{0.5}\text{Mn}_{0.5}\text{O}_2$ ,<sup>[36]</sup>  $\text{K}_3\text{V}_2(\text{PO}_4)_3$ ,<sup>[37]</sup>  $\text{K}_{1.84}\text{Ni}[\text{Fe}(\text{CN})_6]_{0.88}\cdot 0.49\text{H}_2\text{O}$  (KNiHCF),<sup>[28]</sup>  $\text{K}_{1.94}\text{Mn}[\text{Fe}(\text{CN})_6]_{0.994}\cdot 0.08\text{H}_2\text{O}$  (KMF-EDTA),<sup>[13]</sup> and  $\text{KVPO}_4\text{F}$ <sup>[20]</sup>). d) Rate capabilities of the KVP nanorulers, KVP wide nanorulers, and KVP microrods. e) Galvanostatic charge–discharge profiles of the KVP nanorulers under a constant charge current density ( $0.02 \text{ A g}^{-1}$ ) and varied discharge current densities of  $0.02$ – $5 \text{ A g}^{-1}$ . f) Cycling properties of the KVP nanorulers, KVP wide nanorulers, and KVP microrods. g) Ultralong cyclic property of the KVP nanorulers.



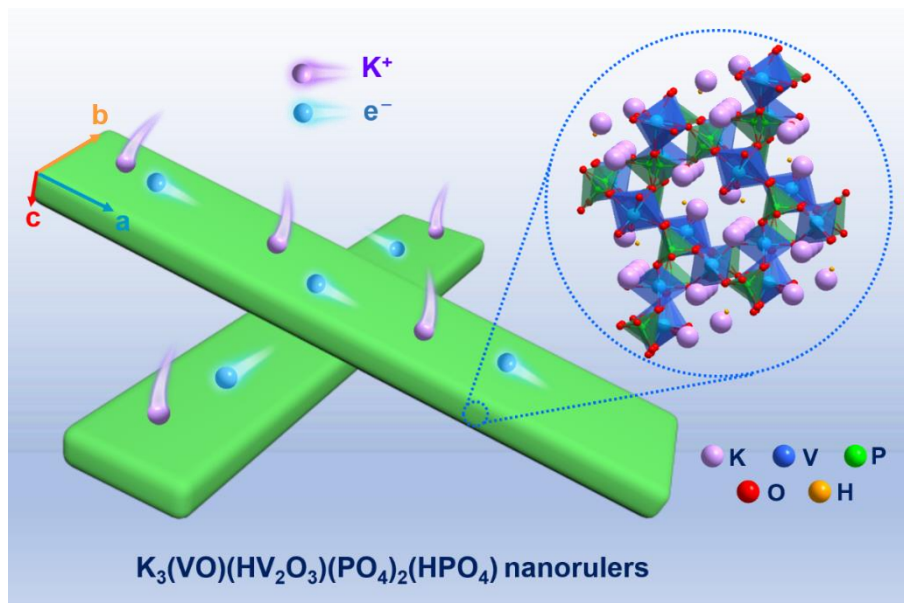
**Figure 4.** a) The voltage curves of the KVP nanorulers in the first two cycles and b) the relevant two-dimensional contour plots of in situ XRD patterns between 13.25–14.25° and 27.5–33.5°. c) Variations of cell volume and lattice parameter computed based on in situ XRD. d),e) V K-edge XANES spectra of the KVP nanorulers at diverse states upon the 10th charging (d) and discharging (e). f) GITT profiles of the KVP nanorulers, KVP wide nanorulers, and KVP microrods. g) Calculated K<sup>+</sup> diffusion pathway in KVP along the *c* orientation. h) K<sup>+</sup> migration energy barriers in KVP along the *a*, *b*, and *c* directions. i) DOS of the KVP in the pristine status.

Accepted Manuscript



**Figure 5.** a) Schematic representation of working mechanism of the KVP nanorulers//PANI-LT full battery. b) Typical depotassiation/potassiation profiles of the full battery. c) Charge–discharge capacities of the full battery at diverse current rates. d) Cyclic stability of the full battery and e) the relevant depotassiation/potassiation profiles of selected cycles.

## for Table of Content Entry



A novel low-strain phosphate cathode material  $K_3(VO)(HV_2O_3)(PO_4)_2(HPO_4)$  (KVP) nanorulers is synthesized by a facile solvothermal approach. The KVP nanorulers manifest high discharge voltage, superior rate capability, and ultralong cyclic life as a cathode material for potassium-ion batteries (PIBs). This work would provide guidance to exploit high-performance PIB cathode materials.